

# Interplay of shell evolution and configuration mixing in the single-hole-like states of $^{99-131}\text{In}$

Deepak Patel <sup>1</sup>, Praveen C. Srivastava <sup>1,\*</sup>, Noritaka Shimizu <sup>2</sup> and Yutaka Utsuno <sup>3,4,†</sup>

<sup>1</sup>*Department of Physics, Indian Institute of Technology Roorkee, Roorkee 247667, India*

<sup>2</sup>*Center for Computational Sciences, University of Tsukuba, 1-1-1, Tennodai Tsukuba, Ibaraki 305-8577, Japan*

<sup>3</sup>*Advanced Science Research Center, Japan Atomic Energy Agency, Tokai, Ibaraki 319-1195, Japan*

<sup>4</sup>*Center for Nuclear Study, University of Tokyo, 7-3-1 Hongo, Bunkyo-ku, Tokyo 113-0033, Japan*

(Dated: January 6, 2025)

Large-scale shell-model calculations are performed for the  $9/2_{g.s.}^+$ ,  $1/2_1^-$ ,  $3/2_1^-$ , and  $5/2_1^-$  states in the odd- $A$  indium isotopes with  $N = 50 - 82$ . The calculated energy levels, electromagnetic moments, and spectroscopic factors exhibit remarkable agreement with the experimental data due to significant configuration mixing for the neutron numbers away from the closed shells. While the  $1/2_1^-$  energy levels well follow those of the effective single-particle energies that are formulated for fractional occupancies of the neutron orbitals, the configuration mixing with the proton  $p_{3/2}$  and  $f_{5/2}$  orbitals plays a crucial role in locating the  $1/2_1^-$  levels at the right position in the actual shell-model calculations.

PACS numbers: 21.60.Cs, 23.20.-g, 23.20.Lv, 27.60.+j

## I. INTRODUCTION

The tin region presents a unique opportunity in nuclear physics [1–14] as the proton magic number  $Z = 50$  allows for the study of the different isotopic chains between two neutron shell closures  $N = 50$  and  $82$ , making it a testing ground to investigate shell evolution [15]. In particular, the isotopes that lie in the neighborhood of the tin, such as indium (In) and antimony (Sb), provide more direct insights into the shell structure due to the occurrence of a single proton hole (particle) outside the proton magic number  $Z = 50$ . For Sb isotopes, Schiffer *et al.* [16] observed a sharp change in the energy level splitting between the  $11/2^-$  and  $7/2^+$  states as the neutron number increases, suggesting a reduction in spin-orbit splitting with neutron excess. This phenomenon was later interpreted by Otsuka *et al.* [17] as evidence of tensor-force-driven shell evolution. However, in another study, Sorlin and Porquet [18] proposed an alternative explanation, attributing this evolution to the coupling of the core excitation. This difference in interpretation is further complicated by different many-body nuclear-structure calculations, such as those by Utsuno *et al.* [19] and Afanasjev *et al.* [20], which either support the shell evolution is driven by tensor-force or the particle-core coupling mechanism, respectively.

Given these contrasting interpretations, it is a natural next step to explore the evolution of single-proton-hole states in In isotopes, particularly with large-scale shell-model calculations [21]. Such studies offer insight into the role of monopole interactions and configuration mixing in shaping nuclear structure properties across isotopic

chains. While cadmium isotopes have been extensively studied to understand the impact of two proton holes relative to the tin core [22–25], indium isotopes, with a single proton hole at  $Z = 49$ , provide a distinct vantage point for examining the evolution of single-proton-like states and their interaction with various neutron configurations. Investigating the structural evolution across indium isotopes may yield a more unified understanding of shell evolution in this region, which could reconcile the observed data from both Sb and In isotopes in terms of the driving forces behind the evolution of nuclear structure.

The present work aims to systematically describe the proton-hole-like levels in In isotopes with large-scale shell-model calculations to deduce the interplay of shell evolution and configuration mixing. We utilize the same proton-neutron interaction as that employed for the study of Sb isotopes [19] on the basis of the  $V_{\text{MU}}$  interaction [26] to provide a consistent description of In isotopes. For this purpose, nuclear energy levels, spectroscopic factors, and nuclear moments in indium isotopes are calculated and compared to the experimental data. In particular, nuclear moments and spectroscopic factors [8, 27] serve as sensitive measures of configuration mixing, providing valuable insights into the mechanisms at play in the structural evolution of these isotopes. We examine the impact of this evolution on the single-proton-hole states  $9/2_{g.s.}^+$ ,  $1/2_1^-$ ,  $3/2_1^-$ , and  $5/2_1^-$ , especially for the  $1/2_1^-$  state, which was not well understood in previous studies.

This paper is organized as follows: In Sec. II, we briefly show the outline of our calculations. In Sec. III, we compare the calculated single-hole-like levels in  $^{99-131}\text{In}$  to the experimental data, and probe the role of configuration mixing through electromagnetic moments and spectroscopic factors. Furthermore, the systematics of the

\* Corresponding author: praveen.srivastava@ph.iitr.ac.in

† utsuno.yutaka@jaea.go.jp

$1/2_1^-$  excitation energies is discussed in terms of shell evolution and correlation energies. Finally, we summarize our results and conclude the paper in Sec. IV.

## II. FORMALISM

The shell-model Hamiltonian  $H$  consists of single-particle energies  $T$  and two-body terms  $V$ ,

$$H = T + V, \quad (1)$$

with

$$T = \sum_{\alpha} \epsilon_{\alpha}^0 \hat{N}_{\alpha}, \quad (2)$$

$$V = \sum_{\alpha \leq \beta, \gamma \leq \delta} V_J(j_{\alpha} j_{\beta} j_{\gamma} j_{\delta}) C_{j_{\alpha} j_{\beta} J M}^{\dagger} C_{j_{\gamma} j_{\delta} J M}. \quad (3)$$

The labels  $\alpha$  to  $\delta$  stand for the set of quantum numbers,  $\alpha = \{\rho_{\alpha} n_{\alpha} l_{\alpha} j_{\alpha}\}$ , where  $\rho = \pi$  for proton or  $\rho = \nu$  for neutron. Instead of  $\alpha$  *etc.*,  $j_{\alpha}$  is often used to label the orbitals as expressed in Eq. (3).  $\hat{N}_{\alpha} = \sum_{m_{\alpha}} c_{\alpha m_{\alpha}}^{\dagger} c_{\alpha m_{\alpha}}$  is the particle number operator, and  $\epsilon_{\alpha}^0$  is the single-particle energy on top of the inert core employed.  $C_{j_{\alpha} j_{\beta} J M}^{\dagger}$  is the pair creation operator,

$$C_{j_{\alpha} j_{\beta} J M}^{\dagger} = \mathcal{N}_{\alpha\beta} \sum_{m_{\alpha} m_{\beta}} (j_{\alpha} m_{\alpha} j_{\beta} m_{\beta} | J M) c_{j_{\alpha} m_{\alpha}}^{\dagger} c_{j_{\beta} m_{\beta}}^{\dagger}, \quad (4)$$

with the normalization factor  $\mathcal{N}_{\alpha\beta} = (1 + \delta_{\alpha\beta})^{-1/2}$ , and  $C_{j_{\alpha} j_{\beta} J M}$  is the Hermitian conjugate of  $C_{j_{\alpha} j_{\beta} J M}^{\dagger}$ . The symbol  $V_J(j_{\alpha} j_{\beta} j_{\gamma} j_{\delta})$  denotes the antisymmetrized two-body matrix elements,  $\langle j_{\alpha} j_{\beta} J M | V | j_{\gamma} j_{\delta} J M \rangle$ , where  $|j_{\alpha} j_{\beta} J M \rangle$  stands for  $C_{j_{\alpha} j_{\beta} J M}^{\dagger} | - \rangle$  with the vacuum  $| - \rangle$ . Note that the value of  $\langle j_{\alpha} j_{\beta} J M | V | j_{\gamma} j_{\delta} J M \rangle$  does not depend on  $M$ , and we omit  $M$  in  $V_J(j_{\alpha} j_{\beta} j_{\gamma} j_{\delta})$ .

In the present study, we performed shell-model calculations for the odd- $A$   $^{99-131}\text{In}$  isotopes. The valence shell consists of four proton orbitals ( $0f_{5/2}$ ,  $1p_{3/2}$ ,  $1p_{1/2}$ , and  $0g_{9/2}$ ) and five neutron orbitals ( $1d_{5/2}$ ,  $2s_{1/2}$ ,  $1d_{3/2}$ ,  $0g_{7/2}$ , and  $0h_{11/2}$ ) with the inert core  $^{78}\text{Ni}$ . The neutron-neutron interaction was taken from the SNBG1 interaction [28], whose matrix elements were semi-empirically determined to reproduce the energy levels of Sn isotopes in the neutron valence shell consisting of ( $1d_{5/2}$ ,  $2s_{1/2}$ ,  $1d_{3/2}$ ,  $0g_{7/2}$ , and  $0h_{11/2}$ ) orbits. The proton-proton interaction is omitted for simplicity because it does not affect the indium isotopes with a proton hole in the valence shell. The proton-neutron interaction was taken from a version of the  $V_{\text{MU}}$  interaction that was employed in the SDPF-MU interaction for the  $sd$ - $pf$  shell [29], in which a two-body spin-orbit interaction was also included. This interaction was also used as the proton-neutron interaction for the study of Sb isotopes [19] with the overall central force scaled by 0.84 to reproduce the binding energies of Sn isotopes. This overall scaling was introduced also in the present study for a consistent description of In

isotopes. All the two-body matrix elements were scaled by  $A^{-0.3}$  following the recipe of the SNBG1 interaction [28]. The single-particle energies of  $0f_{5/2}$ ,  $1p_{3/2}$ ,  $1p_{1/2}$ , and  $0g_{9/2}$  proton orbitals were adjusted so that the corresponding single-hole states in  $^{131}\text{In}$  reported in Ref. [30] could be reproduced. Those of the neutron orbitals were determined to obtain the same energy levels in  $^{101}\text{Sn}$  as those of the SNBG1 interaction. We validated the strength of the interaction by successfully reproducing the experimental proton separation energy difference between  $^{132}\text{Sn}$  and  $^{104}\text{Sn}$ .

For our calculations, the shell-model code KSHELL [31] has been used to diagonalize the shell-model Hamiltonian matrices. We have performed our calculations without any truncation in the present model space. The largest  $M$ -scheme dimension is  $3.4 \times 10^8$  for  $^{115}\text{In}$ .

## III. RESULTS AND DISCUSSIONS

In Sec. III A, we first show the systematics of possible proton-hole-like states ( $9/2_{\text{g.s.}}^+$ ,  $1/2_1^-$ ,  $3/2_1^-$ , and  $5/2_1^-$ ) in  $^{99-131}\text{In}$  and probe their configuration mixing from seniority distribution. In Sec. III B, the obtained configuration mixing is validated with electromagnetic moments. In Sec. III C, we decompose the calculated  $9/2_{\text{g.s.}}^+$  and  $1/2_1^-$  wave functions into the major configurations that are classified according to the hierarchy of energy. The depletion of the single-hole strength is quantified by the spectroscopic factors. In Sec. III D, the systematics of the  $1/2_1^-$  excitation energies is compared to those of the effective single-particle energies, and is accounted for by the interplay of shell evolution and configuration mixing.

### A. Systematics of the $9/2_{\text{g.s.}}^+$ , $1/2_1^-$ , $3/2_1^-$ , and $5/2_1^-$ levels in indium isotopes

In Fig. 1, we compare the calculated energy levels of the  $9/2_1^+$ ,  $1/2_1^-$ ,  $3/2_1^-$ , and  $5/2_1^-$  states with the available experimental data [10, 30, 32] across the odd- $A$  indium isotopic chain. To the best of our knowledge, for the first time in the present work, the experimental trend of  $1/2_1^-$  states throughout the indium chain has been successfully reproduced by shell-model calculations. The comparison in Fig. 1 reveals a generally consistent match between the calculated and experimental trends. For  $^{107,109,113,123,125}\text{In}$ , firm spin-parity assignments of the  $5/2^-$  levels are not provided, and we propose assignments based on the shell-model predictions, as shown in Fig. 1. For  $^{107}\text{In}$ , the shell-model calculation predicts the  $5/2_1^-$  state at 1770 keV. Experimentally, there is an unconfirmed spin-parity state  $(1/2, 3/2, 5/2)^-$  at 1519 keV, and no calculated  $1/2^-$  or  $3/2^-$  states lie in this energy region, leading us to assign the  $5/2_1^-$  state at 1519 keV. Similarly, we have considered that the experimental  $5/2^-$  state at 1441 keV in  $^{109}\text{In}$ ,  $3/2^-$ ,  $5/2^-$  state at 1106 keV

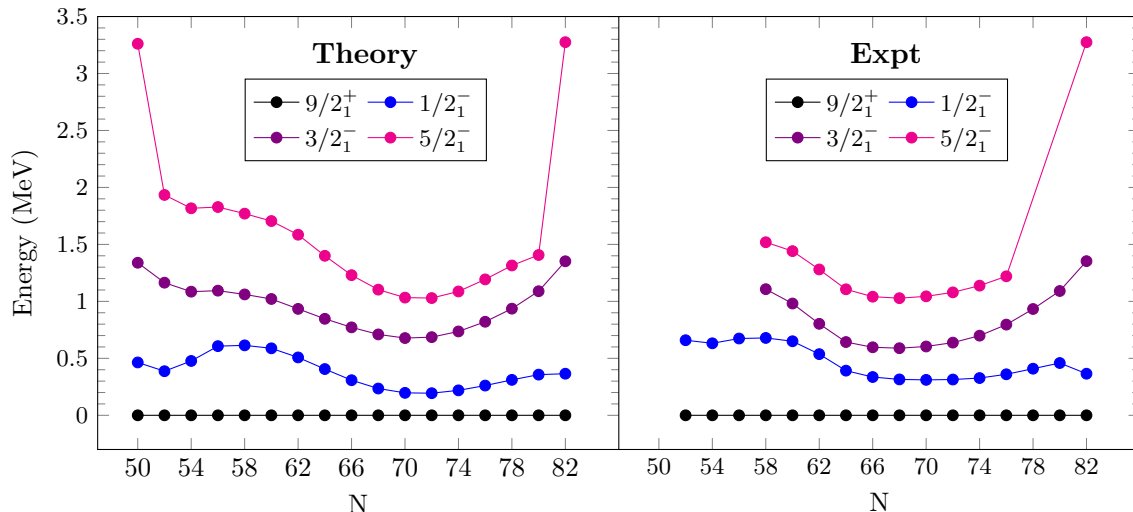


FIG. 1. Comparison of the shell-model energy levels for  $9/2_1^+$ ,  $1/2_1^-$ ,  $3/2_1^-$ , and  $5/2_1^-$  states in odd- $A$  indium isotopes with the experimental data [10, 30, 32].

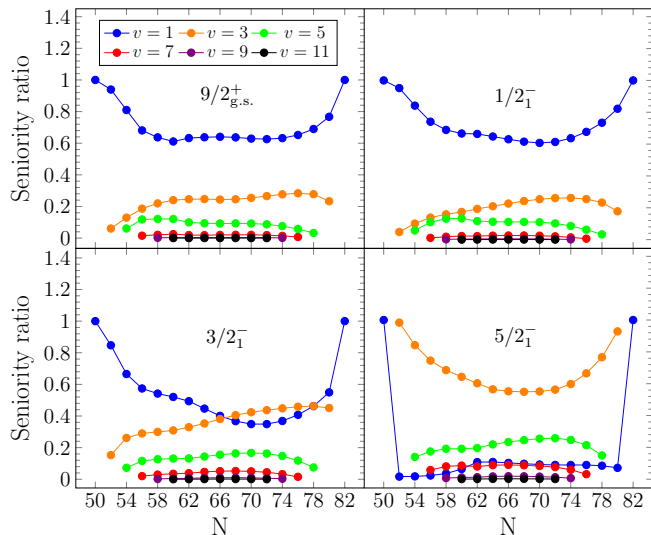


FIG. 2. Seniority of the  $9/2_{g.s.}^+$ ,  $1/2_1^-$ ,  $3/2_1^-$ , and  $5/2_1^-$  states in odd- $A$  indium isotopes.

in  $^{113}\text{In}$ , ( $3/2_1^-, 5/2_1^-$ ) state at 1138 keV in  $^{123}\text{In}$ , and ( $1/2_1^-, 3/2_1^-, 5/2_1^-$ ) state at 1220 keV in  $^{125}\text{In}$  could be the  $5/2_1^-$  states.

The seniority number ( $v$ ) provides useful information on nuclear structure, particularly for examining single-particle structure of a state. It is defined as the unpaired particles, which are not pairwise coupled to the angular momentum  $J = 0$  [33, 34]. In Fig. 2, we illustrate the seniority distribution for the  $9/2_{g.s.}^+$ ,  $1/2_1^-$ ,  $3/2_1^-$ , and  $5/2_1^-$  states across the odd- $A$  indium isotopic chain, highlighting the predominant seniority values for each state. The  $9/2_{g.s.}^+$  and  $1/2_1^-$  states are dominated by  $v = 1$  throughout the isotope chain, thus indicating that the major-

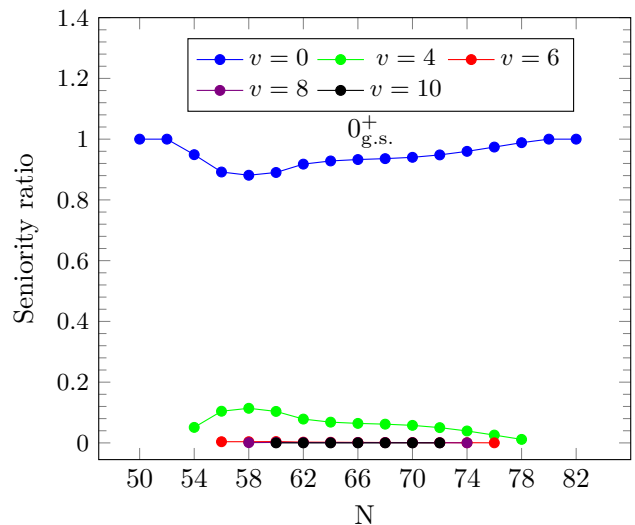


FIG. 3. Seniority of the  $0_{g.s.}^+$  in even- $A$  tin isotopes.

ity of the wave function is composed of a  $\pi(g_{9/2})$  and  $\pi(p_{1/2})$  hole, respectively, on top of the ground states of the corresponding tin isotopes. For the  $3/2_1^-$  and  $5/2_1^-$  states, we observe a different structural behavior. The  $3/2_1^-$  state retains single-particle character across most indium isotopes but shows deviations for isotopes in the after mid-shell region, particularly between  $N = 68 - 76$ , where fragmentation in the wave function leads to the evolution in the collectivity. These deviations are also reflected in the spectroscopic factors discussed later, which suggest a reduced single-particle dominance for this state. On the other hand, the  $5/2_1^-$  state displays a pronounced departure from the single-particle characteristics, except for the neutron shell closures, at  $N = 50$  and  $N = 82$ .

This occurs because the energy of a  $\pi(p_{1/2})$  hole coupled to the  $2_1^+$  state in the corresponding tin isotope is lower than a  $\pi(f_{5/2})$  hole coupled to the ground state for  $52 \leq N \leq 80$ .

In Fig. 3, the seniority distributions of the ground states of tin isotopes are presented to compare those of the  $9/2_{g.s.}^+$ ,  $1/2_1^-$ ,  $3/2_1^-$ , and  $5/2_1^-$  states in indium isotopes shown in Fig. 2. For the tin isotopes, the lowest seniority number ( $v = 0$ ) accounts for  $\gtrsim 90\%$  of the ground state, whereas the corresponding number in the indium isotopes ( $v = 1$ ) is significantly reduced down to  $\sim 60\%$  even for the  $9/2_{g.s.}^+$  and the  $1/2_1^-$  levels. Since the seniority numbers for protons must always be  $v = 1$  in the present model space, this reduction indicates additional configuration mixing driven by a proton hole.

### B. Electromagnetic observables

Here, we discuss the electric quadrupole ( $Q$ ) and magnetic dipole ( $\mu$ ) moments of the proton-hole-like states  $9/2_{g.s.}^+$  and  $1/2_1^-$  in the odd- $A$  indium isotopic chain. These two observables are important to probe the effect of configuration mixing and extract information about the nature of wave functions [35]. Here, we mainly focus on studying the systematics of electric quadrupole and magnetic moment of  $9/2_{g.s.}^+$ ; the theoretical and experimental comparisons of  $Q(9/2_{g.s.}^+)$  and  $\mu(9/2_{g.s.}^+)$  values are depicted in Fig. 4. Also, the theoretical and experimental data for  $Q(9/2_{g.s.}^+)$ ,  $\mu(9/2_{g.s.}^+)$ , and  $\mu(1/2_1^-)$  values are reported in Table I.

We consider two distinct sets of effective charges ( $e_p, e_n$ ), as  $(1.6, 0.8)e$  and  $(1.56, 1.04)e$ . The first set has been used in previous studies [23, 36], while the latter is determined through a chi-square fitting method. In this procedure, the neutron effective charge ( $1.04e$ ) is first derived using the theoretical and corresponding experimental  $B(E2; 2_1^+ \rightarrow 0_{g.s.}^+)$  transition strengths in Sn isotopes. Subsequently, with the neutron effective charge fixed, the optimal proton effective charge ( $1.56e$ ) has been obtained utilizing the theoretical and experimental quadrupole moments of the  $9/2_{g.s.}^+$  in indium isotopes. The shell-model calculations predict positive  $Q$  values for  $9/2_{g.s.}^+$  across the  $^{99-131}\text{In}$  chain, demonstrating a consistent trend as the neutron number increases. The gradual change in  $Q$  values reflects structural evolution with neutron number due to significant configuration mixing in the mid-shell region, while the decrement near neutron shell closures indicates changes from the collective behavior to the single-particle nature and clear reduction in the nuclear charge polarization [8]. The overall agreement between theoretical and experimental  $Q(9/2_{g.s.}^+)$  values, especially with effective charges  $(1.56, 1.04)e$  (see upper panel of Fig. 4), indicates that the shell-model interaction used in these calculations effectively captures the primary characteristics of the  $9/2_{g.s.}^+$  in the indium isotopes.

In the lower panel of Fig. 4, we have plotted the

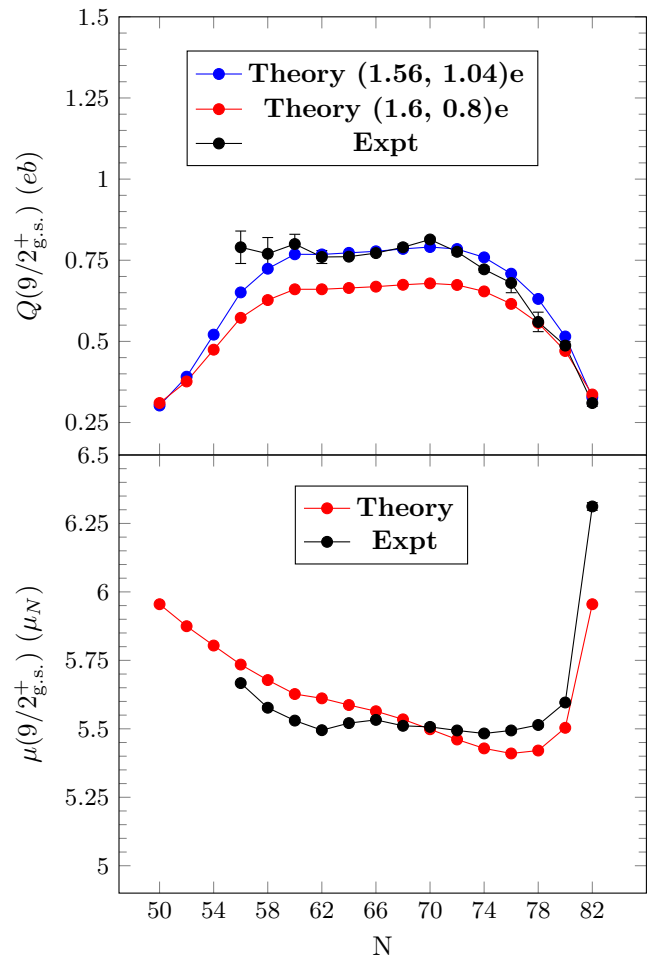


FIG. 4. Comparison between the calculated and experimental [37, 38] electric quadrupole (upper) and magnetic dipole (lower) moment of  $9/2_{g.s.}^+$  for odd- $A$  indium isotopes.

shell-model predicted and experimental magnetic moment  $\mu(9/2_{g.s.}^+)$  in  $^{99-131}\text{In}$  for comparison. The effective  $g$  factors we take are  $(g_l^p, g_l^n) = (1.0, 0.0)$  and  $(g_s^p, g_s^n) = (3.910, -2.678)$  for the orbital and spin angular momenta, respectively, following Ref. [23]. The experimental magnetic moments are quite stable except at  $N = 82$ . The present calculations well reproduce this property, but show a shallow minimum at  $N = 76$  in contrast to the experimental data. We reasonably reproduce the abrupt increment in  $\mu(9/2_{g.s.}^+)$  at  $N = 82$ , whereas the difference between the  $N = 82$  and the  $N = 80$  is not completely reproduced. As indicated by the seniority variation (see Fig. 2), the proton hole drives additional configuration mixing for  $9/2_{g.s.}^+$  in the indium isotopes away from shell closures, leading to a reduced  $\mu(9/2_{g.s.}^+)$  value. A detailed analysis of the configuration mixing is discussed later.

Further, the observed magnetic moment of  $1/2_1^-$  state decreases with the increase of neutron number up to  $^{125}\text{In}$  and beyond that increases in the  $^{127-131}\text{In}$  iso-

TABLE I. Electric quadrupole and magnetic moments of odd- $A$  indium isotopes. In our calculations we have taken two sets of effective charges  $(e_p, e_n) = (1.6, 0.8)e$  [36] and  $(1.56, 1.04)e$ ; the gyromagnetic ratios for the spin angular momenta are taken as  $g_s^p = 3.910$  and  $g_s^n = -2.678$ , and those for the orbital angular momenta are  $g_l^p = 1.0$  and  $g_l^n = 0.0$  [23].

$A$	$J^\pi$	$Q$ (eb)				$\mu$ ( $\mu_N$ )		
		Theory		Expt. [37]	Expt. [38]	Theory	Expt. [37]	Expt. [38]
		$(1.6, 0.8)e$	$(1.56, 1.04)e$					
99	$9/2_1^+$	0.310	0.302	-	-	5.955	-	-
	$1/2_1^-$	-	-	-	-	0.015	-	-
101	$9/2_1^+$	0.377	0.391	-	-	5.875	-	-
	$1/2_1^-$	-	-	-	-	-0.022	-	-
103	$9/2_1^+$	0.474	0.521	-	-	5.804	-	-
	$1/2_1^-$	-	-	-	-	-0.079	-	-
105	$9/2_1^+$	0.573	0.651	0.79(5)	-	5.735	5.667(5)	-
	$1/2_1^-$	-	-	-	-	-0.120	-	-
107	$9/2_1^+$	0.627	0.724	0.77(5)	-	5.678	5.577(8)	-
	$1/2_1^-$	-	-	-	-	-0.139	-	-
109	$9/2_1^+$	0.661	0.768	0.80(3)	-	5.627	5.530(4)	-
	$1/2_1^-$	-	-	-	-	-0.158	-	-
111	$9/2_1^+$	0.661	0.768	0.76(2)	-	5.611	5.495(7)	-
	$1/2_1^-$	-	-	-	-	-0.180	-	-
113	$9/2_1^+$	0.665	0.773	0.761(5)	0.767(27)	5.587	5.5208(4)	5.5264(19)
	$1/2_1^-$	-	-	-	-	-0.201	-0.21043(3)	-0.21(1)
115	$9/2_1^+$	0.669	0.778	0.772(5)	0.784(42)	5.564	5.5326(4)	5.541(2)
	$1/2_1^-$	-	-	-	-	-0.220	-0.24362(5)	-0.2405(38)
117	$9/2_1^+$	0.674	0.785	0.790(10)	0.807(22)	5.535	5.511(4)	5.5286(43)
	$1/2_1^-$	-	-	-	-	-0.237	-0.25136(4)	-0.2766(27)
119	$9/2_1^+$	0.679	0.791	0.814(7)	0.794(23)	5.498	5.507(10)	5.499(62)
	$1/2_1^-$	-	-	-	-	-0.250	-0.319(5)	-0.342(12)
121	$9/2_1^+$	0.674	0.785	0.776(10)	0.803(23)	5.461	5.494(5)	5.575(62)
	$1/2_1^-$	-	-	-	-	-0.260	-0.354(4)	-0.3600(41)
123	$9/2_1^+$	0.654	0.759	0.722(9)	0.736(23)	5.429	5.483(7)	5.442(61)
	$1/2_1^-$	-	-	-	-	-0.266	-0.399(4)	-0.4047(54)
125	$9/2_1^+$	0.616	0.709	0.68(3)	0.673(24)	5.410	5.494(9)	5.496(24)
	$1/2_1^-$	-	-	-	-	-0.263	-0.432(4)	-0.450(17)
127	$9/2_1^+$	0.557	0.631	0.56(3)	0.588(29)	5.421	5.514(8)	5.5321(14)
	$1/2_1^-$	-	-	-	-	-0.241	-	-0.4355(24)
129	$9/2_1^+$	0.470	0.515	-	0.487(13)	5.504	-	5.5961(23)
	$1/2_1^-$	-	-	-	-	-0.167	-	-0.38709(58)
131	$9/2_1^+$	0.336	0.328	-	0.31(1)	5.955	-	6.312(14)
	$1/2_1^-$	-	-	-	-	0.015	-	-0.0514(48)

topes. Shell-model calculated  $\mu$ -moments for  $1/2^-$  are slightly higher than the observed values but show almost the same trend as in the experimental data.

Similar to the effective charges, effective  $g$  factors can be determined by the chi-square fitting. The resulting agreement with the experimental data is, however, not significantly improved, and the obtained proton  $g$  factors deviate from the standard values. To avoid such an overfitting, we have presented in Fig. 4 and Table I the calculated magnetic moments only with the  $g$  factors in accordance with the systematics.

We have also calculated the root mean square (rms) deviation in both observables ( $Q$  and  $\mu$ ) using the formula given as follows

$$\text{rms} = \sqrt{\frac{1}{N} \sum_{k=1}^N (W_{\text{expt}}^k - W_{\text{th}}^k)^2}. \quad (5)$$

Here,  $W_{\text{expt}}^k$  and  $W_{\text{th}}^k$  denote the experimental and theoretical observables, respectively. In the calculation of rms deviation, the experimental data for  $Q(9/2_{\text{g.s.}}^+)$  and  $\mu(9/2_{\text{g.s.}}^+)$  in  $^{129,131}\text{In}$ , and  $\mu(1/2_1^-)$  in  $^{127-131}\text{In}$  are taken from Ref. [38]. All other experimental data for  $Q$  and  $\mu$  values are taken from Ref. [37]. By considering the maximum experimental uncertainties in  $Q$ -moments, the estimated rms deviations corresponding to the effective charges  $(1.6, 0.8)e$  and  $(1.56, 1.04)e$  are  $0.110_{-0.019}^{+0.021}$  and  $0.048_{-0.003}^{+0.014}$  eb, respectively. Similarly, our computed rms deviation for  $\mu$ -moments is  $0.1209_{-0.0004}^{+0.0008} \mu_N$ . These val-

TABLE II. The calculated  $B(E2)$  and  $B(M1)$  transitions between the low-lying proton-hole-like states in indium isotopes compared to the experimental data [39]. The effective  $E2$  and  $M1$  operators are the same as those used for Table I.

Isotope	Transition ( $J_i^\pi \rightarrow J_f^\pi$ )	$B(E2)$ (W.u.)		Expt.	$B(M1)$ (W.u.)	
		Theory			Theory	Expt.
		(1.6, 0.8) $e$	(1.56, 1.04) $e$			
$^{109}\text{In}$	$3/2_1^- \rightarrow 1/2_1^-$	12.2	16.7	-	0.39	$0.96_{-31}^{+30}$
$^{111}\text{In}$	$5/2_1^- \rightarrow 1/2_1^-$	14.6	21.7	$0.47 >$		
$^{115}\text{In}$	$3/2_1^- \rightarrow 1/2_1^-$	14.5	20.7	-	0.38	$\geq 0.0047$

ues are quite small, which shows a good descriptive power of these observables in the present shell-model calculations.

In Table II, we have also presented the shell-model predicted  $B(E2)$  and  $B(M1)$  transitions for those proton-hole-like states where at least a limit for the experimental data are available in any transition mode ( $B(E2)$  or  $B(M1)$ ).

### C. Configuration mixing in the single-hole-like states and spectroscopic factors

Here, we carry out more detailed analyses of the configuration mixing caused by a proton hole for the  $9/2_{g.s.}^+$  and the  $1/2_1^-$  levels. The dominant configurations of

these states are naturally  $[\pi(g_{9/2})^{-1} \times 0_1^+]^{(9/2^+)}$  and  $[\pi(p_{1/2})^{-1} \times 0_1^+]^{(1/2^-)}$ , respectively, for which  $0_1^+$  stands for the ground state of the tin isotope with the same neutron number. Now we dub these configurations the leading order (LO) configurations, because both the proton and the neutron wave functions have the lowest energies in their respective model spaces. In this context, the configurations with either the proton or the neutron ones excited from the lowest state can be regarded as the next leading order (NLO) configurations. Typical excitation energies of protons and those of neutrons are both  $\sim 1$  MeV or more. Since the proton excited states, i.e.,  $\pi(p_{3/2})^{-1}$  and  $\pi(f_{5/2})^{-1}$ , cannot produce  $9/2^+$  or  $1/2^-$  states by coupling to the  $0_1^+$  state, the NLO configurations consist only of the neutron excited states. The resulting NLO configurations can be given by  $[\pi(g_{9/2})^{-1} \times J_k^+]^{(9/2^+)}$  and  $[\pi(p_{1/2})^{-1} \times J_k^+]^{(1/2^-)}$  ( $J_k^+ \neq 0_1^+$ ) for the  $9/2_{g.s.}^+$  and the  $1/2_1^-$  states, respectively. It is then natural to define the next-to-next leading order (N2LO) configurations as those with both the proton and the neutron configurations excited from the lowest states, which include all the configurations in the present model space except the LO or NLO configurations.

In the actual shell-model calculations, the energies of the LO configurations can be calculated by using two-body Hamiltonian matrix elements and the occupation numbers in the ground states of tin isotopes, as we will present the formula as Eq. (18) in Sec. III D. To evaluate the lowest energies in the LO+NLO configurations in a practical way, we perform shell-model calculations with a proton hole restricted to either the  $p_{1/2}$  or the  $g_{9/2}$  orbital. Note that some of the N2LO configurations, such as  $[\pi(p_{1/2})^{-1} \times 5_1^-]^{9/2^+}$  for  $9/2^+$ , are admixed in this calculation but that their contributions are much smaller compared to the majority of the NLO configurations. The N2LO configurations can be included by carrying out shell-model calculations in the full model space employed in this study.

The effects of the higher order configurations on the  $1/2_1^-$  levels in indium isotopes are shown in Fig. 5. While the excitation energies in the LO are rather constant and are not far from the experimental data along the isotope chain, those in the LO+NLO increase for

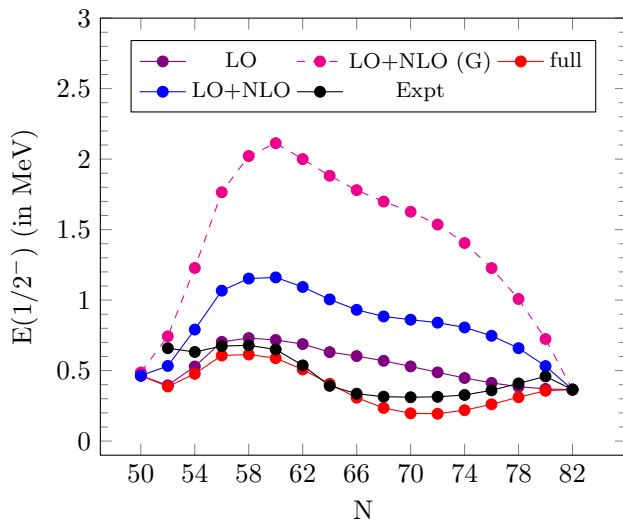


FIG. 5. Evolution of the experimental  $1/2_1^-$  levels in odd- $A$  indium isotopes (Expt) compared to those of theory with different levels of configuration mixing included. The LO, LO+NLO, and full stand for the degrees of configuration mixing with the present effective interaction employed, and the LO+NLO (G) is the LO+NLO model space with the  $G$ -matrix based proton-neutron interaction that is used in Ref. [23]. See the text for details.

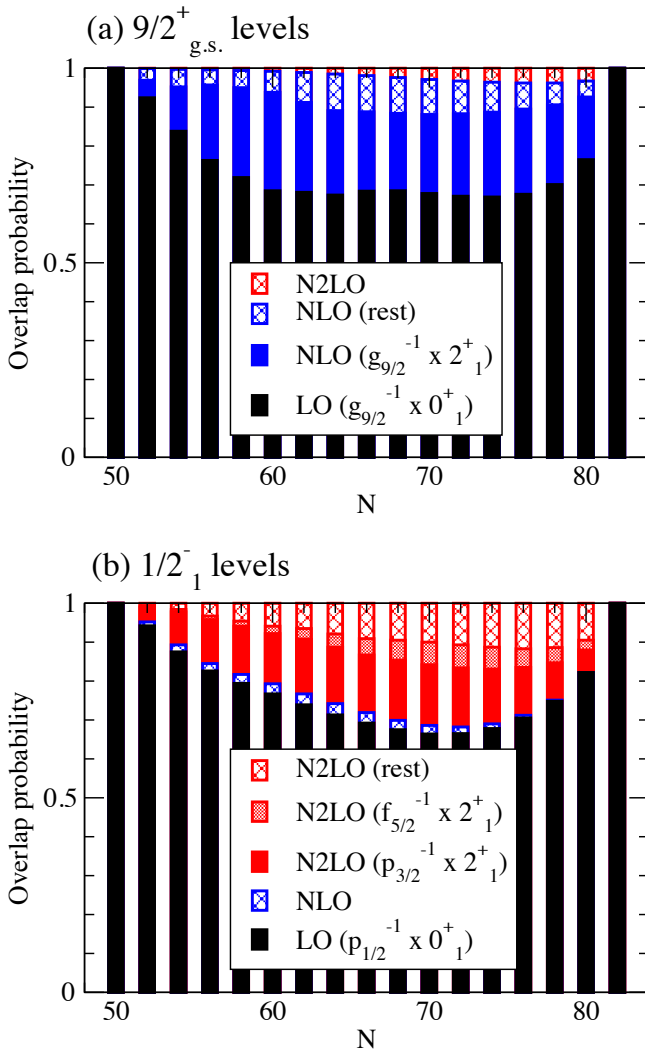


FIG. 6. Overlap probabilities of (a) the  $9/2^+_{g.s.}$  and (b) the  $1/2^-_{1}$  states with a few dominant configurations. See the text for the notation of the configurations.

the neutron number away from the closed shells. As a result, a considerable deviation from the experimental levels arises. As denoted by LO+NLO (G) in Fig. 5, this trend is similar but more enhanced with a  $G$ -matrix based proton-neutron interaction [23] used in the same model space. This indicates that the deviation in the LO+NLO is, aside from how much the energy increases, predominantly due to the degrees of restriction of the model space. By including the N2LO configurations in the full model space, the  $1/2^-_{1}$  levels are lowered from those of the LO+NLO, and become very close to the experimental data on the whole.

Here we pursue why the  $1/2^-_{1}$  levels behave as shown in Fig. 5 by enlarging the model space. First, we compare the  $1/2^-_{1}$  energy levels in the LO to those in the LO+NLO. As mentioned already, the NLO configurations are  $[\pi(g_{9/2})^{-1} \times J_k^+]^{(9/2^+)}$  and  $[\pi(p_{1/2})^{-1} \times J_k^+]^{(1/2^-)}$  for the  $9/2^+_{g.s.}$  and the  $1/2^-_{1}$  states, respectively. Here, the

possible quantum number  $J$  is limited to make a  $9/2^+$  or  $1/2^-$  state after the proton and the neutron angular momenta are coupled. More specifically, neutron states with  $0 \leq J \leq 9$  are possible for  $9/2^+$ , whereas only those of  $0 \leq J \leq 1$  are allowed for  $1/2^-$ . In particular, the coupling to the  $2^+_{1}$  state, which is expected to be the largest fraction in the NLO because of the lowest excited state, is missing in the latter. As a result, the coupling to the NLO lowers the energies of the  $9/2^+_{g.s.}$  more than those of the  $1/2^-_{1}$  states, thus increasing the  $1/2^-_{1}$  excitation energies.

Next, we compare the  $1/2^-_{1}$  energy levels in the LO+NLO to those of the full configurations in which states with a proton hole in the  $p_{3/2}$  or the  $f_{5/2}$  orbital are also activated. The key to shifting the excitation energies of the  $1/2^-_{1}$  states is parity coupling. For constructing the  $9/2^+_{g.s.}$ , the coupling of the  $p_{3/2}$  or the  $f_{5/2}$  proton hole to a negative-parity state is allowed but the coupling to a positive-parity state is prohibited. The situation for the  $1/2^-_{1}$  state is opposite. Since low-lying states in tin isotopes are dominated by positive-parity states, the coupling to N2LO configurations is larger for the  $1/2^-_{1}$  states than for the  $9/2^+_{g.s.}$ , decreasing the excitation energies of the  $1/2^-_{1}$  states.

As thus discussed, not only the NLO configurations but also the N2LO configurations play a significant role in the  $1/2^-_{1}$  excitation energies because the former and the latter configurations selectively favor the  $9/2^+_{g.s.}$  and the  $1/2^-_{1}$  states, respectively. This situation is clearly seen from Fig. 6, in which dominant configurations in the  $9/2^+_{g.s.}$  and the  $1/2^-_{1}$  states are contrasted. The  $1/2^-_{1}$  excitation energies lowered by the N2LO configurations almost cancel those raised by the NLO configurations. As a result of this process, the  $1/2^-_{1}$  levels are located at the right positions. This fact is worth attention because shell-model calculations are often carried out in the proton valence shell that consists of the  $p_{1/2}$  and the  $g_{9/2}$  orbitals [23, 40–44], i.e., in the LO+NLO in our notation.

The overlap probabilities between an eigenstate and a specific configuration, such as those presented in Fig. 6, can be probed with the spectroscopic factor that is deduced from nucleon transfer or knockout reactions. Here, an eigenstate with mass number  $A$  is denoted as  $|\alpha\rangle = |\Psi^A \omega J M\rangle$ , where  $J$  and  $M$  are the total angular momentum and its  $z$  component, respectively, and  $\omega$  is introduced to label the state with the same  $(J, M)$ . The hole state with the same quantum numbers is expressed as  $|\beta\rangle = \mathcal{N} [\tilde{c}_j \times |\Psi^{A+1} \omega' J' M'\rangle]^{(J)}_M$ , where  $\mathcal{N}$  is the normalization factor, and  $\tilde{c}_{jm} = (-1)^{j+m} c_{j-m}$  is the hole creation operator. The overlap between  $|\alpha\rangle$  and  $|\beta\rangle$  is

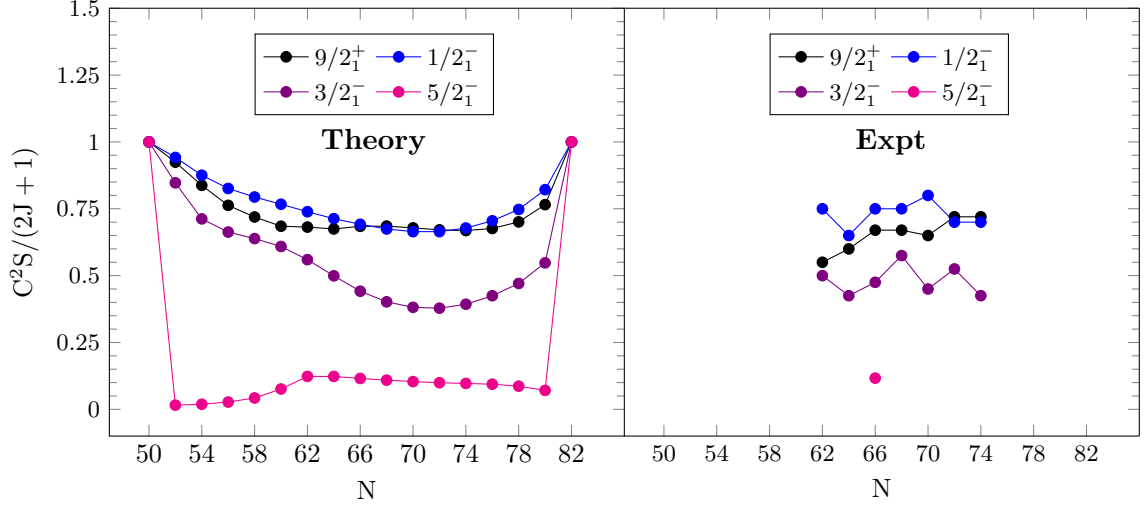


FIG. 7. Comparison of the shell-model predicted and experimental spectroscopic factors ( $C^2S$ ) divided by  $2J + 1$  for  $9/2_{g.s.}^+$ ,  $1/2_1^-$ ,  $3/2_1^-$ , and  $5/2_1^-$  states.

represented as

$$\begin{aligned}
 \langle \beta | \alpha \rangle &= \mathcal{N} \sum_{mM'} (jmJ'M' | JM) (-1)^{j+m} \\
 &\quad \times \langle \Psi^{A+1} \omega' J' M' | c_j^\dagger | \Psi^A \omega J M \rangle \\
 &= \mathcal{N} \sum_{mM'} \sqrt{2J+1} \begin{pmatrix} j & J' & J \\ m & M' & -M \end{pmatrix}^2 \\
 &\quad \times \langle \Psi^{A+1} \omega' J' | c_j^\dagger | \Psi^A \omega J \rangle \\
 &= \mathcal{N} \frac{\langle \Psi^{A+1} \omega' J' | c_j^\dagger | \Psi^A \omega J \rangle}{\sqrt{2J+1}}.
 \end{aligned} \quad (6)$$

The corresponding overlap probability is expressed as

$$|\langle \beta | \alpha \rangle|^2 = \mathcal{N}^2 \frac{2J'+1}{2J+1} C^2 S_j(\omega J, \omega' J'), \quad (7)$$

using the spectroscopic factor defined as

$$C^2 S_j(\omega J, \omega' J') = \frac{|\langle \Psi^{A+1} \omega' J' | c_j^\dagger | \Psi^A \omega J \rangle|^2}{2J'+1}, \quad (8)$$

where  $\omega J$  and  $\omega' J'$  are to designate the initial and the final states we take. If not necessary, these labels are omitted, and the spectroscopic factors are then simply denoted as  $C^2 S_j$  or  $C^2 S$ . In the present study, we consider the situation in which a proton hole is created by  $\tilde{c}_{jm}$  ( $j = g_{9/2}, p_{1/2}, p_{3/2}, f_{5/2}$ ) on top of the fully occupied states,  $\pi(f_{5/2})^6(p_{3/2})^4(p_{1/2})^2(g_{9/2})^{10}$ . In such a case, the normalization factor  $\mathcal{N}$  is always unity, and the overlap probability given by Eq. (7) can directly be deduced from the spectroscopic factor. The cumulative sum of the overlap probabilities of the LO and NLO configurations is the sum of  $|\langle \beta | \alpha \rangle|^2$  over all the states in the tin isotopes with the hole state  $j$  fixed (to  $\pi g_{9/2}$  for the  $9/2_1^+$  level or to  $\pi p_{1/2}$  for the  $1/2_1^-$  level). Hence for  $\mathcal{N} = 1$  it reads

$$\begin{aligned}
 \sum_{\omega' J'} |\langle \beta | \alpha \rangle|^2 &= \sum_{\omega' J'} \frac{2J'+1}{2J+1} C^2 S_j(\omega J, \omega' J') \\
 &= (2j+1) - n_j(\alpha),
 \end{aligned} \quad (9)$$

where  $n_j(\alpha)$  stands for the nucleon occupation number in the orbital  $j$  for the state  $|\alpha\rangle$ . The overlap probabilities plotted in Fig. 6 are thus obtained with the  $C^2S$  and the  $n_j(\alpha)$  values in the KSHELL outputs.

The experimental  $C^2S$  values for  $9/2_{g.s.}^+$ ,  $1/2_1^-$ ,  $3/2_1^-$ , and  $5/2_1^-$  states are available from the one-proton pick-up reaction  $^{A+1}\text{Sn}(d, ^3\text{He})^A\text{In}$  for stable tin isotopes. The results of the theoretical and experimental  $C^2S$  values are summarized in Table III. The experimental values for the  $9/2_{g.s.}^+$ ,  $1/2_1^-$ , and  $3/2_1^-$  states in  $^{115-123}\text{In}$ ,  $^{111}\text{In}$  and  $^{113}\text{In}$  are taken from Ref. [27], Ref. [45], and Ref. [46], respectively. The experimental value for the  $5/2_1^-$  state in  $^{115}\text{In}$  is taken from Ref. [47].

The calculated  $C^2S$  values for the  $9/2_{g.s.}^+$ ,  $1/2_1^-$ ,  $3/2_1^-$ , and  $5/2_1^-$  states show remarkable agreement with the available experimental data. To emphasize to what extent the single-hole nature is kept in these states, we plot these  $C^2S$  values divided by  $2J + 1$  in Fig. 7, which is identical with the overlap probabilities of the LO configuration, as shown in Eq. (7) (Note that  $J' = 0$ ). It is known that the experimental spectroscopic factors, especially the overall factor, cannot be free from some systematic uncertainties because deducing the spectroscopic factors relies on reaction theories. As seen in Fig. 7, the experimental  $C^2S$  values stagger with neutron number compared to smooth evolutions predicted by theory. It is most likely that this staggering is due to the experimental uncertainties, although the experimental error bars are not provided. By considering the experimental uncertainties, the theory well captures what the experimental data tell us: (i) The  $C^2S/(2J + 1)$  values for the  $9/2_{g.s.}^+$  and the  $1/2_1^-$  states are about 0.7 in the mid-shell, pointing to significant configuration mixing even for the lowest two states. (ii) The  $C^2S/(2J + 1)$  values for the  $3/2_1^-$  are reduced to

TABLE III. Comparison of the shell-model calculated spectroscopic factors ( $C^2S$ ) for low-lying states of odd- $A$  indium isotopes with the experimental data [27, 45–47] from the  $A+1\text{Sn}(d,^3\text{He})^A\text{In}$  reactions.

Isotope	$J^\pi$	Theory (keV)	Expt. (keV)	L	$C^2S$	
					SM	Expt.
$^{99}\text{In}$	$9/2_{\text{g.s.}}^+$	0	-	4	10.000	-
	$1/2_1^-$	464	-	1	2.000	-
	$3/2_1^-$	1339	-	1	4.000	-
$^{101}\text{In}$	$5/2_1^-$	3261	-	3	6.000	-
	$9/2_{\text{g.s.}}^+$	0	0	4	9.243	-
	$1/2_1^-$	387	659	1	1.884	-
$^{103}\text{In}$	$3/2_1^-$	1164	-	1	3.388	-
	$5/2_1^-$	1934	-	3	0.094	-
	$9/2_{\text{g.s.}}^+$	0	0	4	8.376	-
$^{105}\text{In}$	$1/2_1^-$	477	632	1	1.751	-
	$3/2_1^-$	1085	-	1	2.849	-
	$5/2_1^-$	1817	-	3	0.114	-
$^{107}\text{In}$	$9/2_{\text{g.s.}}^+$	0	0	4	7.628	-
	$1/2_1^-$	607	674	1	1.652	-
	$3/2_1^-$	1094	-	1	2.652	-
$^{109}\text{In}$	$5/2_1^-$	1828	-	3	0.163	-
	$9/2_{\text{g.s.}}^+$	0	0	4	7.193	-
	$1/2_1^-$	614	679	1	1.588	-
$^{111}\text{In}$	$3/2_1^-$	1061	1107	1	2.554	-
	$5/2_1^-$	1770	1519	3	0.255	-
	$9/2_{\text{g.s.}}^+$	0	0	4	6.848	-
$^{113}\text{In}$	$1/2_1^-$	588	650	1	1.534	-
	$3/2_1^-$	1021	981	1	2.436	-
	$5/2_1^-$	1705	1441	3	0.456	-
$^{115}\text{In}$	$9/2_{\text{g.s.}}^+$	0	0	4	6.815	5.5
	$1/2_1^-$	508	537	1	1.478	1.5
	$3/2_1^-$	934	803	1	2.239	2
$^{117}\text{In}$	$5/2_1^-$	1585	1280	3	0.739	-
	$9/2_{\text{g.s.}}^+$	0	0	4	6.746	6.0
	$1/2_1^-$	406	392	1	1.426	1.3
$^{119}\text{In}$	$3/2_1^-$	847	647	1	1.997	1.7
	$5/2_1^-$	1400	1106	3	0.738	-
	$9/2_{\text{g.s.}}^+$	0	0	4	6.844	6.7
$^{121}\text{In}$	$1/2_1^-$	308	336	1	1.384	1.5
	$3/2_1^-$	772	597	1	1.767	1.9
	$5/2_1^-$	1230	1041	3	0.693	0.7
$^{123}\text{In}$	$9/2_{\text{g.s.}}^+$	0	0	4	6.852	6.7
	$1/2_1^-$	235	315	1	1.349	1.5
	$3/2_1^-$	710	589	1	1.608	2.3
$^{125}\text{In}$	$5/2_1^-$	1103	1028	3	0.655	-
	$9/2_{\text{g.s.}}^+$	0	0	4	6.785	6.5
	$1/2_1^-$	197	311	1	1.329	1.6
$^{127}\text{In}$	$3/2_1^-$	678	604	1	1.526	1.8
	$5/2_1^-$	1033	1044	3	0.622	-
	$9/2_{\text{g.s.}}^+$	0	0	4	6.712	7.2
$^{129}\text{In}$	$1/2_1^-$	194	314	1	1.329	1.4
	$3/2_1^-$	686	638	1	1.513	2.1
	$5/2_1^-$	1029	1079	3	0.597	-
$^{131}\text{In}$	$9/2_{\text{g.s.}}^+$	0	0	4	6.685	7.2
	$1/2_1^-$	219	327	1	1.356	1.4
	$3/2_1^-$	736	699	1	1.572	1.7
$^{133}\text{In}$	$5/2_1^-$	1087	1138	3	0.581	-

TABLE III. (Continued)

Isotope	$J^\pi$	Theory (keV)	Expt. (keV)	L	$C^2S$	
					SM	Expt.
$^{125}\text{In}$	$9/2_{\text{g.s.}}^+$	0	0	4	6.763	-
	$1/2_1^-$	261	360	1	1.410	-
	$3/2_1^-$	821	796	1	1.699	-
$^{127}\text{In}$	$5/2_1^-$	1193	1220	3	0.564	-
	$9/2_{\text{g.s.}}^+$	0	0	4	7.010	-
	$1/2_1^-$	311	409	1	1.495	-
$^{129}\text{In}$	$3/2_1^-$	936	933	1	1.883	-
	$5/2_1^-$	1315	-	3	0.520	-
	$9/2_{\text{g.s.}}^+$	0	0	4	7.655	-
$^{131}\text{In}$	$1/2_1^-$	357	459	1	1.643	-
	$3/2_1^-$	1089	1091	1	2.191	-
	$5/2_1^-$	1407	-	3	0.425	-
$^{133}\text{In}$	$9/2_{\text{g.s.}}^+$	0	0	4	10.000	-
	$1/2_1^-$	365	365	1	2.000	-
	$3/2_1^-$	1352	1353	1	4.000	-
$^{135}\text{In}$	$5/2_1^-$	3275	3275	3	6.000	-

$\sim 0.5$ , indicating further depletion of the single-hole strengths. (iii) The  $C^2S/(2J+1)$  value for the  $5/2_1^-$  in  $^{115}\text{In}$  is only  $\sim 0.1$ , suggesting the dominance of a collective state,  $\pi(p_{1/2})^{-1} \times 2_1^+$ .

#### D. Effective single-hole energies

While significant configuration mixing occurs in the  $9/2_{\text{g.s.}}^+$ ,  $1/2_1^-$ ,  $3/2_1^-$  and  $5/2_1^-$  states as seen already, proton single-hole characters still remain particularly in the  $9/2_{\text{g.s.}}^+$  and the  $1/2_1^-$  states. Hence it is worth examining the systematics of these energies in terms of shell evolution.

In the shell model, shell evolution is characterized by the effective single-particle energy (ESPE). For a fully occupied orbital  $j$ , the ESPE is defined as the energy that is needed to add a nucleon hole in the orbital  $j$  by using the monopole interaction [15]. In the present case, we consider the  $Z = 50$  core, for which the effective proton single-hole energies  $\epsilon(j_p^{-1})$  for a state with  $n_{j_n}$  neutrons occupying the orbitals  $j_n$  are given by

$$\begin{aligned} \epsilon(j_p^{-1}) &= \epsilon^0(j_p^{-1}) + \sum_{j_n} V_{pn}^m(j_p^{-1}, j_n) n_{j_n} \\ &= \epsilon^0(j_p^{-1}) - \sum_{j_n} V_{pn}^m(j_p, j_n) n_{j_n}, \end{aligned} \quad (10)$$

where  $V_{pn}^m(j_p, j_n)$  is the monopole matrix element between  $j_p$  and  $j_n$  given by

$$\begin{aligned} V_{pn}^m(j_p, j_n) &= \frac{\sum_{J=|j_p-j_n|}^{j_p+j_n} (2J+1) V_J(j_p j_n j_p j_n)}{\sum_{J=|j_p-j_n|}^{j_p+j_n} (2J+1)} \\ &= \frac{\sum_{J=|j_p-j_n|}^{j_p+j_n} (2J+1) V_J(j_p j_n j_p j_n)}{(2j_p+1)(2j_n+1)}, \end{aligned} \quad (11)$$

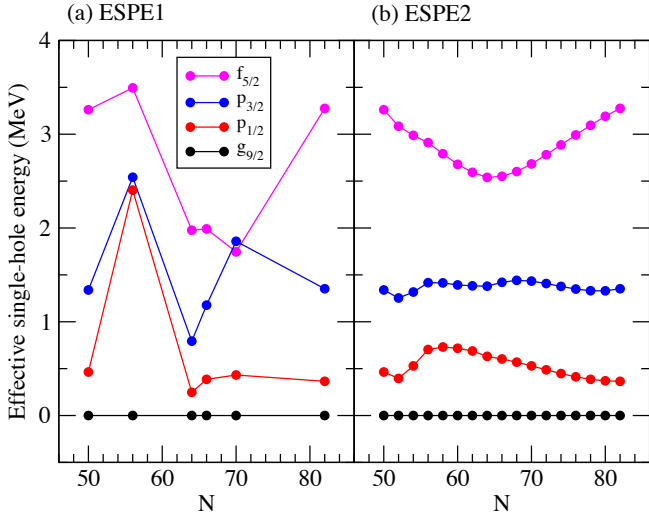


FIG. 8. Proton effective single-hole energies of the  $g_{9/2}$ ,  $p_{1/2}$ ,  $p_{3/2}$  and  $f_{5/2}$  orbitals with the definitions of (a) ESPE1 and (b) ESPE2, measured from those of  $g_{9/2}$ . For ESPE1, it is assumed that neutrons fill the orbitals in the order of  $d_{5/2}$ ,  $g_{7/2}$ ,  $s_{1/2}$ ,  $d_{3/2}$  and  $h_{11/2}$ .

and  $\epsilon^0(j_p^{-1})$  is the bare single-hole energy of  $j_p$ . The diagonal matrix element of the particle-hole interaction is represented by using the Pandya transformation [48] as

$$V_J(j_p^{-1}j_nj_p^{-1}j_n) = -\sum_{J'}(2J'+1) \left\{ \begin{matrix} j_p & j_n & J' \\ j_p & j_n & J \end{matrix} \right\} V_{J'}(j_pj_nj_pj_n), \quad (12)$$

from which  $V_{pn}^m(j_p^{-1}, j_n) = -V_{pn}^m(j_p, j_n)$  is derived, and is used in Eq. (10).

To obtain effective proton single-particle (or single-hole) energies, one often assumes that each neutron orbital  $j_n$  is either completely vacant or completely occupied, i.e.,  $n_n = 0$  or  $n_n = 2j_n + 1$ . Here, we dub this conventional effective single-particle energy ESPE1. However, Eq. (10) can also be applied to fractional neutron occupancies. The natural choice for defining such generalized effective proton single-hole energies, which we call ESPE2, is to use the neutron occupancies of the ground state of the tin isotope with the same neutron number.

The proton effective single-hole energies measured from  $g_{9/2}$  are illustrated in Fig. 8. Here, we focus on the evolution of excitation energies of the  $p_{1/2}$  proton hole. When the orbital  $j_n$  is filled by  $n_{j_n}$  neutrons, the excitation energy changes by

$$\Delta = (V_{pn}^m(g_{9/2}, j_n) - V_{pn}^m(p_{1/2}, j_n)) n_{j_n}. \quad (13)$$

As discussed in Ref. [15], the central and the tensor forces give major contributions to the monopole matrix elements. The central force produces a large negative monopole matrix element between two orbitals  $(n_1l_1j_1)$  and  $(n_2l_2j_2)$  for  $n_1 = n_2$ , and the latter gives attraction when  $(j_1, j_2) = (l_1 + 1/2, l_2 - 1/2)$  or  $(j_1, j_2) =$

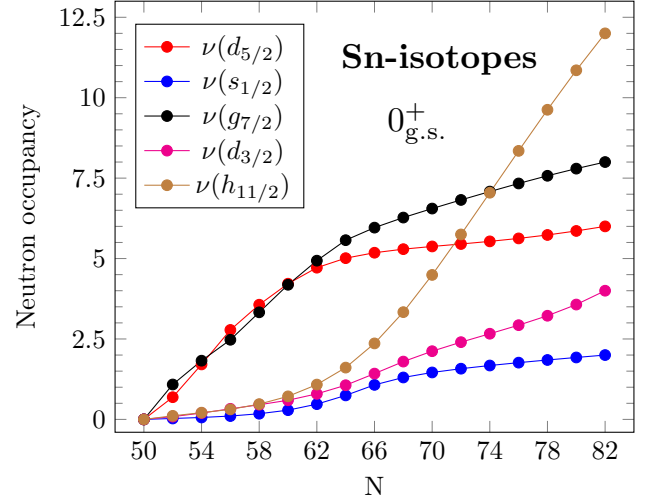


FIG. 9. Neutron occupancy for the  $0_{g.s.}^+$  in even- $A$  tin isotopes.

TABLE IV. Labeling several pairs of the orbitals  $(j_p, j_n)$  of interest according to the strengths of the monopole matrix elements  $V_{pn}^m(j_p, j_n)$  by the central and the tensor forces. The labels “f”, “u” and “0” stand for the favored (most attractive), unfavored (less attractive or repulsive), and vanishing matrix elements, respectively. The first and the second labels are for the central and the tensor forces, respectively.

$j_p \backslash j_n$	$1d_{5/2}$	$0g_{7/2}$	$2s_{1/2}$	$1d_{3/2}$	$0h_{11/2}$
$0g_{9/2}$	(u, u)	(f, f)	(u, 0)	(u, f)	(f, u)
$1p_{1/2}$	(f, f)	(u, u)	(u, 0)	(f, u)	(u, f)

$(l_1 - 1/2, l_2 + 1/2)$  is satisfied. These general properties are applied to the neutron and the proton orbitals of interest, resulting in the labels summarized in Table IV. From these labels, one easily finds that the  $p_{1/2}$  proton hole excitation energy sharply increase and decrease when neutrons fill the  $d_{5/2}$  and  $g_{7/2}$  orbitals, respectively. The other neutron orbitals produce similar effects on the  $g_{9/2}$  and the  $p_{1/2}$  proton orbitals. The  $p_{1/2}$  proton hole excitation energy is kept almost constant when these neutron orbitals are filled. The behavior of the  $p_{1/2}$  proton hole excitation energy presented in Fig. 8 (a) is thus understood.

The proton effective single-hole energies defined as ESPE2 are depicted in Fig. 8 (b). The sharp peak at  $N = 56$  seen in Fig. 8 (a) disappears, and the  $p_{1/2}$  proton hole excitation energy changes much milder. This is due to the actual neutron occupancies shown in Fig. 9: Neutrons predominantly fill the  $d_{5/2}$  and  $g_{7/2}$  orbitals almost equally for  $N \lesssim 64$  because of their similar single-particle energies and a large pairing matrix element of  $V_{J=0}(d_{5/2}d_{5/2}g_{7/2}g_{7/2})$ , and then fill the remaining orbitals for  $N \gtrsim 64$ . As a result, the opposite effects of the neutron  $d_{5/2}$  and  $g_{7/2}$  orbitals on the proton  $g_{9/2}$  and  $p_{1/2}$  are almost canceled out.

In the following, we prove that the excitation energies due to the ESPE2 is identical with the those of the LO configuration of the corresponding orbitals, as shown in Fig. 5. To calculate the energy of the LO configuration, the proton hole state is expressed as

$$\Phi_{j_p m_p} = d_{j_p m_p}^\dagger \Psi(0_1^+), \quad (14)$$

where  $d_{j_p m_p}^\dagger = \tilde{c}_{j_p m_p} = (-1)^{j_p+m_p} c_{j_p -m_p}$  is the proton-hole creation operator and  $\Psi(0_1^+)$  is the ground state of the tin core. The expectation value of the Hamiltonian for  $\Phi_{j_p m_p}$  is written as

$$\begin{aligned} E(j_p m_p) &= \langle \Phi_{j_p m_p} | H | \Phi_{j_p m_p} \rangle \\ &= \epsilon^0(j_p^{-1}) + \langle \Phi_{j_p m_p} | V_{pn} | \Phi_{j_p m_p} \rangle \\ &\quad + \langle \Psi(0_1^+) | H_{nn} | \Psi(0_1^+) \rangle, \end{aligned} \quad (15)$$

where  $V_{pn}$  and  $H_{nn}$  are the proton-neutron interaction and the neutron sector of the Hamiltonian, respectively. From Eq. (3), the  $V_{pn}$  is expressed as

$$\begin{aligned} V_{pn} &= \sum_{j'_p j''_p j'_n j''_n m'_p m''_p m'_n m''_n JM} V_J ((j'_p)^{-1} j''_p (j'_n)^{-1} j''_n) \\ &\quad \times (j'_p m'_p j'_n m'_n | JM) (j''_p m''_p j''_n m''_n | JM) \\ &\quad \times d_{j'_p m'_p}^\dagger c_{j'_n m'_n}^\dagger c_{j''_n m''_n} c_{j''_p m''_p}, \end{aligned} \quad (16)$$

with the particle-hole matrix elements  $V_J ((j'_p)^{-1} j''_p (j'_n)^{-1} j''_n)$ . Its expectation value for  $\Phi_{j_p m_p}$  is calculated to be

$$\begin{aligned} &\langle \Phi_{j_p m_p} | V_{pn} | \Phi_{j_p m_p} \rangle \\ &= \sum_{m_p} \frac{\langle \Phi_{j_p m_p} | V_{pn} | \Phi_{j_p m_p} \rangle}{2j_p + 1} \\ &= \sum_{j'_n m'_n JM m_p} \frac{V_J (j_p^{-1} j'_n j_p^{-1} j'_n)}{2j_p + 1} \\ &\quad \times (j_p m_p j'_n m'_n | JM)^2 \langle \Psi(0_1^+) | c_{j'_n m'_n}^\dagger c_{j'_n m'_n} | \Psi(0_1^+) \rangle \\ &= \sum_{J j'_n} \frac{(2J+1) V_J (j_p^{-1} j'_n j_p^{-1} j'_n)}{(2j_p+1)(2j'_n+1)} n_{j'_n} \\ &= \sum_{j'_n} V_{pn}^m(j_p^{-1}, j'_n) n_{j'_n} \\ &= - \sum_{j'_n} V_{pn}^m(j_p, j'_n) n_{j'_n}, \end{aligned} \quad (17)$$

with  $n_{j'_n} = \langle \Psi(0_1^+) | \sum_{m'_n} c_{j'_n m'_n}^\dagger c_{j'_n m'_n} | \Psi(0_1^+) \rangle$ . The first equality of Eq. (17) is nothing but the fact that the energy does not depend on  $m_p$ . The second equality is obtained by assuming that there is no pair of the neutron orbitals with the same angular momentum and parity in the valence shell, such as  $1d_{5/2}$  and  $2d_{5/2}$ , resulting in  $\langle \Psi(0_1^+) | c_{j'_n m'_n}^\dagger c_{j'_n m'_n} | \Psi(0_1^+) \rangle = \delta_{j'_n j'_n} \delta_{m'_n m'_n} \langle \Psi(0_1^+) | c_{j'_n m'_n}^\dagger c_{j'_n m'_n} | \Psi(0_1^+) \rangle$ , and by using  $\langle - | d_{j_p m_p}^\dagger d_{j'_p m'_p}^\dagger d_{j''_p m''_p}^\dagger d_{j_p m_p} | - \rangle = \delta_{j_p j'_p} \delta_{j_p j''_p} \delta_{m_p m'_p} \delta_{m_p m''_p}$  for the vacuum  $| - \rangle$ . The third equality follows the orthogonality of the Clebsch-Gordan coefficient,  $\sum_{M m_p} (j_p m_p j'_n m'_n | JM)^2 = (2J+1)/(2j'_n+1)$ . Hence, Eq. (15) is written as

$$E(j_p m_p) = \epsilon^0(j_p^{-1}) - \sum_{j'_n} V_{pn}^m(j_p, j'_n) n_{j'_n} + E_{nn}, \quad (18)$$

with  $E_{nn} = \langle \Psi(0_1^+) | H_{nn} | \Psi(0_1^+) \rangle$ . Since  $E_{nn}$  does not depend on the proton hole state  $(j_p, m_p)$ , we do not have to consider it when only the relative energy,  $E(j_p m_p) - E(j'_p m'_p)$ , is of interest. As a result, Eq. (18) is the same as Eq. (10) when its neutron part is ignored.

In the way we demonstrated above, the evolution of the  $1/2_1^-$  excitation energies in the LO configuration, which is identical with the  $p_{1/2}$  proton hole excitation energies in ESPE2, should be rather mild because of the almost equal filling of neutrons in  $d_{5/2}$  and  $g_{7/2}$  in the lower mass tin isotopes. A very similar trend is obtained if the proton-neutron interaction is replaced with the  $G$ -matrix based one that was used in Ref. [23]. It is thus most likely that the difference between LO+NLO and LO+NLO (G) in Fig. 5 occurs predominantly because the coupling energies of the LO and the NLO configurations is larger with the  $G$  matrix interaction than with the  $V_{MU}$  interaction. The  $1/2_1^-$  energy levels must be more or less peaked independently of the interaction in the LO+NLO configurations as seen in Fig. 5, and the experimental excitation energies can only be reproduced with the N2LO configurations included, i.e., with shell-model calculations including the  $\pi p_{3/2}$  and the  $\pi f_{5/2}$  orbitals as the valence shell.

#### IV. SUMMARY AND CONCLUSIONS

We have investigated the interplay of shell evolution and configuration mixing in the proton-hole-like states in  $^{99-131}\text{In}$  with large-scale shell-model calculations in the the proton and neutron model spaces of  $Z = 28 - 50$  and  $N = 50 - 82$ , respectively. The proton-neutron effective interaction, which is essential in shell evolution, is taken from a variant of the  $V_{MU}$  interaction for a consistent description of the proton-particle-like states in  $^{101-133}\text{Sb}$  that were studied previously. The calculated energy levels of the  $1/2_1^-$ ,  $3/2_1^-$ , and  $5/2_1^-$  states with respect to the  $9/2_{g.s.}^+$  are in a remarkable agreement with the experimental data. The evolution of the electromagnetic moments in the  $9/2_{g.s.}^+$  and the  $1/2_1^-$  levels is also well reproduced, indicating significant configuration mixing in these states for the neutron number away from the closed shells.

To gain more insight into the configuration mixing in these levels, the wave functions are decomposed into several dominant configurations that are classified according to the order of energy. The single-hole strengths of the  $9/2_{g.s.}^+$  and the  $1/2_1^-$  states are both reduced to  $\sim 0.7$  toward the mid-shell, which is supported by the measured spectroscopic factors taken from the  $^{A+1}\text{Sn}(d, ^3\text{He})^A\text{In}$  reactions. On the other hand, the rest configurations show unique features: (i) As for the next-leading configurations in terms of energy, the  $\pi(g_{9/2})^{-1} \times 2_1^+$  configuration occupies a large fraction of the  $9/2_{g.s.}^+$ , but the corresponding configuration in the  $1/2_1^-$  states, i.e.,  $\pi(p_{1/2})^{-1} \times 2_1^+$ , cannot make  $J = 1/2$  and is therefore excluded. (ii) The  $\pi(p_{3/2})^{-1} \times 2_1^+$  and  $\pi(f_{5/2})^{-1} \times 2_1^+$  con-

figurations can be mixed with the negative-parity states, but are excluded from admixture in the  $9/2_{\text{g.s.}}^+$  due to the parity conservation. Although the effects of (ii) are regarded as the next-to-next leading order in terms of energy, its energy gain is comparable to that of (i). As a result, the effects of (i) and (ii) on the  $1/2_1^-$  excitation energies are almost canceled out, which makes these excitation energies close to the effective proton single-hole energies. The  $\pi p_{1/2}$  effective single-hole energies measured from those of  $\pi g_{9/2}$  should change rather mildly along  $N = 50 - 82$ , following the general properties of the monopole matrix elements of the central and tensor forces, and the nearly equal filling of the  $\nu d_{5/2}$  and  $\nu g_{7/2}$  orbitals for the lower neutron numbers. The evolution of the  $1/2_1^-$  levels is thus obtained as a subtle interplay between shell evolution and configuration mixing. In particular, it is worth pointing out that these energies should deviate from the data without the  $\pi p_{3/2} - \pi f_{5/2}$  orbitals

because of the missing correlation energy due to (ii).

## ACKNOWLEDGMENTS

We acknowledge financial support from MHRD, the Government of India, and SERB (India), CRG/2022/005167. We would like to thank the National Supercomputing Mission (NSM) for providing computing resources of ‘PARAM Ganga’ at the Indian Institute of Technology Roorkee, implemented by C-DAC and supported by MeitY and DST, Government of India. N.S. and Y.U. acknowledge the support of “Program for promoting researches on the supercomputer Fugaku,” MEXT, Japan (Grant No. JPMXP1020230411), and the support of JSPS KANENHI Grant No. 20K03981. N.S. acknowledges the MCRP program of the Center for Computational Sciences, University of Tsukuba (NUCLSM).

- 
- [1] K. L. Jones, A. S. Adekola, D. W. Bardayan, J. C. Blackmon, K. Y. Chae *et al.*, The magic nature of  $^{132}\text{Sn}$  explored through the single-particle states of  $^{133}\text{Sn}$ , *Nature* **465**, 454 (2010).
- [2] C. Gorges, L. V. Rodríguez, D. L. Balabanski, M. L. Bissell, K. Blaum *et al.*, Laser Spectroscopy of Neutron-Rich Tin Isotopes: A Discontinuity in Charge Radii across the  $N = 82$  Shell Closure, *Phys. Rev. Lett.* **122**, 192502 (2019).
- [3] T. D. Morris, J. Simonis, S. R. Stroberg, C. Stumpf, G. Hagen *et al.*, Structure of the Lightest Tin Isotopes, *Phys. Rev. Lett.* **120**, 152503 (2018).
- [4] N. J. Stone, D. Doran, M. Lindroos, J. Rikowska, M. Veskovic *et al.*, Magnetic Moments of Odd- $A$  Sb Isotopes to  $^{133}\text{Sb}$ : Significant Evidence for Mesonic Exchange Current Contributions and on Core Collective  $g$  Factors, *Phys. Rev. Lett.* **78**, 820 (1997).
- [5] M. Górska, L. Cáceres, H. Grawe, M. Pfützner, A. Jungclauss *et al.*, Evolution of the  $N = 82$  shell gap below  $^{132}\text{Sn}$  inferred from core excited states in  $^{131}\text{In}$ , *Phys. Lett. B* **672**, 313 (2009).
- [6] D. A. Nesterenko, J. Ruotsalainen, M. Stryjczyk, A. Kankainen, L. Al Ayoubi *et al.*, High-precision measurements of low-lying isomeric states in  $^{120-124}\text{In}$  with the JYFLTRAP double Penning trap, *Phys. Rev. C* **108**, 054301 (2023).
- [7] J. Hakala, J. Dobaczewski, D. Gorelov, T. Eronen, A. Jokinen *et al.*, Precision Mass Measurements beyond  $^{132}\text{Sn}$ : Anomalous Behavior of Odd-Even Staggering of Binding Energies, *Phys. Rev. Lett.* **109**, 032501 (2012).
- [8] A. R. Vernon, R. F. Garcia Ruiz, T. Miyagi, C. L. Binnersley, J. Billowes *et al.*, Nuclear moments of indium isotopes reveal abrupt change at magic number 82, *Nature* **607**, 260 (2022).
- [9] D. T. Yordanov, L. V. Rodríguez, D. L. Balabanski, J. Bieroń, M. L. Bissell *et al.*, Structural trends in atomic nuclei from laser spectroscopy of tin, *Commun Phys* **3**, 107 (2020).
- [10] X. Xu, J. H. Liu, C. X. Yuan, Y. M. Xing, M. Wang *et al.*, Masses of ground and isomeric states of  $^{101}\text{In}$  and configuration-dependent shell evolution in odd- $A$  indium isotopes, *Phys. Rev. C* **100**, 051303(R) (2019).
- [11] Z. Q. Chen, Z. H. Li, H. Hua, H. Watanabe, C. X. Yuan *et al.*, Proton Shell Evolution below  $^{132}\text{Sn}$ : First Measurement of Low-Lying  $\beta$ -Emitting Isomers in  $^{123,125}\text{Ag}$ , *Phys. Rev. Lett.* **122**, 212502 (2019).
- [12] M. Spieker, P. Petkov, E. Litvinova, C. Müller-Gatermann, S. G. Pickstone *et al.*, Shape coexistence and collective low-spin states in  $^{112,114}\text{Sn}$  studied with the  $(p, p'\gamma)$  Doppler-shift attenuation coincidence technique, *Phys. Rev. C* **97**, 054319 (2018).
- [13] D. T. Yordanov, D. L. Balabanski, M. L. Bissell, K. Blaum, I. Budinčević *et al.*, Simple Nuclear Structure in  $^{111-129}\text{Cd}$  from Atomic Isomer Shifts, *Phys. Rev. Lett.* **116**, 032501 (2016).
- [14] A. Kankainen, J. Hakala, T. Eronen, D. Gorelov, A. Jokinen *et al.*, Isomeric states close to doubly magic  $^{132}\text{Sn}$  studied with the double Penning trap JYFLTRAP, *Phys. Rev. C* **87**, 024307 (2013).
- [15] T. Otsuka, A. Gade, O. Sorlin, T. Suzuki, and Y. Utsuno, Evolution of shell structure in exotic nuclei, *Rev. Mod. Phys.* **92**, 015002 (2020).
- [16] J. P. Schiffer, S. J. Freeman, J. A. Caggiano, C. Deibel, A. Heinz *et al.*, Is the Nuclear Spin-Orbit Interaction Changing with Neutron Excess? *Phys. Rev. Lett.* **92**, 162501 (2004).
- [17] T. Otsuka, T. Suzuki, R. Fujimoto, H. Grawe, and Y. Akaishi, Evolution of Nuclear Shells due to the Tensor Force, *Phys. Rev. Lett.* **95**, 232502 (2005).
- [18] O. Sorlin, and M.-G. Porquet, Nuclear magic numbers: New features far from stability, *Prog. Part. Nucl. Phys.* **61**, 602 (2008).
- [19] Y. Utsuno, T. Otsuka, N. Shimizu, M. Honma, T. Mizusaki *et al.*, Recent shell-model results for exotic nuclei, *EPJ Web of Conferences* **66**, 02106 (2014).
- [20] A. V. Afanasjev, and E. Litvinova, Impact of collective vibrations on quasiparticle states of open-shell odd-mass

- nuclei and possible interference with the tensor force, *Phys. Rev. C* **92**, 044317 (2015).
- [21] E. Caurier, G. M-Pinedo, F. Nowacki, A. Poves, and A. P. Zuker, The shell model as a unified view of nuclear structure, *Rev. Mod. Phys.* **77**, 427 (2005).
- [22] A. P. Zuker, Quadrupole dominance in the light Sn and in the Cd isotopes, *Phys. Rev. C* **103**, 024322 (2021).
- [23] D. Patel, P. C. Srivastava, N. Shimizu, and Y. Utsuno, Systematic shell-model study of  $^{99-129}\text{Cd}$  isotopes and isomers in neutron-rich  $^{127-131}\text{In}$  isotopes, *Phys. Rev. C* **109**, 014310 (2024).
- [24] D. T. Yordanov, D. L. Balabanski, J. Bieroń, M. L. Bissell, K. Blaum *et al.*, Spins, Electromagnetic Moments, and Isomers of  $^{107-129}\text{Cd}$ , *Phys. Rev. Lett.* **110**, 192501 (2013).
- [25] M. Siciliano, J. J. Valiente-Dobón, A. Goasduff, T. R. Rodríguez, D. Bazzacco *et al.*, Lifetime measurements in the even-even  $^{102-108}\text{Cd}$  isotopes, *Phys. Rev. C* **104**, 034320 (2021).
- [26] T. Otsuka, T. Suzuki, M. Honma, Y. Utsuno, N. Tsunoda *et al.*, Novel Features of Nuclear Forces and Shell Evolution in Exotic Nuclei, *Phys. Rev. Lett.* **104**, 012501 (2010).
- [27] C. V. Weiffenbach, and R. Tickle, Structure of Odd- $A$  Indium Isotopes Determined by the  $(d, ^3\text{He})$  Reaction, *Phys. Rev. C* **3**, 1668 (1971).
- [28] M. Honma, T. Otsuka, T. Mizusaki, Y. Utsuno, N. Shimizu, and M. Hjorth-Jensen, Shell-model study of nuclear structure around  $^{100}\text{Sn}$ , *RIKEN Accel. Prog. Rep.* **47**, 64 (2014).
- [29] Y. Utsuno, T. Otsuka, B. A. Brown, M. Honma, T. Mizusaki, and N. Shimizu, Shape transitions in exotic Si and S isotopes and tensor-force-driven Jahn-Teller effect, *Phys. Rev. C* **86**, 051301(R) (2012).
- [30] V. Vaquero, A. Jungclaus, T. Aumann, J. Tscheuschner, E. V. Litvinova *et al.*, Fragmentation of Single-Particle Strength around the Doubly Magic Nucleus  $^{132}\text{Sn}$  and the Position of the  $0f_{5/2}$  Proton-Hole State in  $^{131}\text{In}$ , *Phys. Rev. Lett.* **124**, 022501 (2020).
- [31] N. Shimizu, T. Mizusaki, Y. Utsuno and Y. Tsunoda, Thick-restart block Lanczos method for large-scale shell-model calculations, *Comput. Phys. Comm.* **244**, 372 (2019).
- [32] Evaluated Nuclear Structure Data File (ENSDF) <http://www.nndc.bnl.gov/ensdf/>.
- [33] G. Racah, Theory of Complex Spectra. III, *Phys. Rev.* **63**, 367 (1943).
- [34] B. H. Flowers, Studies in  $jj$ -coupling. I. Classification of nuclear and atomic states, *Proc. R. Soc. Lond. A* **212**, 248 (1952).
- [35] A. Bohr, and B. R. Mottelson, Nuclear Structure Volume I: Single-Particle Motion, *World Scientific Publishing Co. Pte. Ltd.* (1998).
- [36] M. Honma, T. Otsuka, T. Mizusaki, Y. Utsuno, N. Shimizu, and M. Hjorth-Jensen, Shell-model description of magnetic dipole bands in  $^{105}\text{Sn}$ , *RIKEN Accel. Prog. Rep.* **51**, 95 (2018).
- [37] Nuclear Electromagnetic Moments Compilation - IAEA NDS [www-nds.iaea.org/nuclearmoments/](http://www-nds.iaea.org/nuclearmoments/).
- [38] A. R. Vernon, Collinear Resonance Ionization Spectroscopy of Neutron-Rich Indium Isotopes, *Springer The- ses* (2020).
- [39] NuDat 3 - National Nuclear Data Center, [https://www.nndc.bnl.gov/nudat3/indx\\_adopted.jsp](https://www.nndc.bnl.gov/nudat3/indx_adopted.jsp).
- [40] D. Kast, A. Jungclaus, K.P. Lieb, M. Górska, G. de Angelis *et al.*, Lifetime study of high-spin states in  $^{104,105}\text{In}$ , *EPJ A* **3**, 115 (1998).
- [41] J. Kownacki, M. Lipoglavšek, L.-O. Norlin, J. Nyberg, D. Seweryniak *et al.*, High-spin studies of the neutron deficient nuclei  $^{103}\text{In}$ ,  $^{105}\text{In}$ ,  $^{107}\text{In}$ , and  $^{109}\text{In}$ , *Nucl. Phys. A* **627**, 239 (1997).
- [42] N. Boelaert, N. Smirnova, K. Heyde, and J. Jolie, Shell model description of the low-lying states of the neutron deficient Cd isotopes, *Phys. Rev. C* **75**, 014316 (2007).
- [43] N. Boelaert, A. Dewald, C. Fransen, J. Jolie, A. Linne- mann *et al.*, Low-spin electromagnetic transition probabilities in  $^{102,104}\text{Cd}$ , *Phys. Rev. C* **75**, 054311 (2007).
- [44] D. Patel, P. C. Srivastava, and N. Shimizu, Systematic shell-model study of  $^{98-130}\text{Cd}$  isotopes and  $8^+$  isomeric states, *Nucl. Phys. A* **1039**, 122742 (2023).
- [45] J. Blachot, Nuclear Data Sheets for  $A = 111$ , *Nucl. Data Sheets* **110**, 1239 (2009).
- [46] J. Blachot, Nuclear Data Sheets for  $A = 113$ , *Nucl. Data Sheets* **111**, 1471 (2010).
- [47] J. Blachot, Nuclear Data Sheets for  $A = 115$ , *Nucl. Data Sheets* **113**, 2391 (2012).
- [48] S. P. Pandya, Nucleon-Hole Interaction in  $jj$  Coupling, *Phys. Rev.* **103**, 956 (1956).